

Acoustic Topological Transport and Refraction in a Kekulé Lattice


Boyang Xie,¹ Hui Liu,¹ Hua Cheng,^{1,3} Zhengyou Liu,² Shuqi Chen,^{1,3,4,*} and Jianguo Tian^{1,3}

¹*The Key Laboratory of Weak Light Nonlinear Photonics, Ministry of Education, School of Physics and TADA Institute of Applied Physics, Nankai University, Tianjin 300071, China*

²*School of Physics and Technology and Institute for Advanced Studies, Wuhan University, Wuhan 430072, China*

³*Renewable Energy Conversion and Storage Center, Nankai University, Tianjin 300071, China*

⁴*The collaborative Innovation Center of Extreme Optics, Shanxi University, Taiyuan, Shanxi 030006, China*

 (Received 11 November 2018; revised manuscript received 18 February 2019; published 26 April 2019)

Exploration of topology in photonic and sonic crystals has inspired a number of intriguing phenomena, such as backscattering-immune and defect-insensitive transport at domain walls. Instead of introducing topological gauge flux, the topological insulator realized by the pseudospin Hall effect exhibits extraordinary advantages in acoustics, in which the noise caused by flow is avoided. Here, we report on the experimental observation of the topological transport of sound in a sonic crystal with a Kekulé lattice. With different designs of the domain walls, pseudospin-Hall or valley-Hall edge states emerge around either Γ or K point of the Brillouin zone. Through spatial scanning the sound field, the parity and the angular selectivity of the edge states are visualized. Our work provides an alternative way towards the design of directional antennas for sound.

DOI: [10.1103/PhysRevApplied.11.044086](https://doi.org/10.1103/PhysRevApplied.11.044086)

I. INTRODUCTION

In recent years, artificial microstructures including sonic crystals, metamaterials and metasurfaces have revolutionized the field of sound modulations. The sonic crystals and metamaterials, which consist of periodic arranged units, have demonstrated lots of promising applications, including negative-index or zero-index materials [1–3], rectifier [4], unidirectional transmission [5,6], deep-subwavelength imaging [7], and cloaking [8]. Metasurfaces that serve as planar metamaterials, have also exhibited a practical prospect in wavefront manipulations, exploiting the generalized Snell law [9,10]. However, the scalar nature of the acoustic wave has restricted acoustic device design. By mimicking the quantum effects, the parameter space in acoustic device design can be greatly extended. Intrinsic to conic dispersions, quantum phenomena such as extremal transmission [11], Zitterbewegung oscillations [12], and especially topological transport are proposed. Topological concepts such as quantum Hall effects [13,14], quantum spin Hall effects [15–19] and valley Hall effects [20,21] have opened up new avenues to research sonic systems. Recently, Weyl points and Fermi arcs have been proposed in stacked sonic crystals [22–25], mimicking the quantum Hall effects in three-dimensional systems.

Besides the backscattering-immune transport that has been intensively investigated, the outcoupling of

topological edge states have also shown its prospect for application. The topologically protected refraction has recently been demonstrated in valley crystals [26–30], which is fundamentally different from ordinary plane-wave refraction at the Brewster angle. Similar to the anomalous refraction that has been intensely researched in the field of metamaterials [9,10], the refraction angle can be solved by phase-matching condition at the terminal interface. Compared to previously acoustic beam splitters without topological effects [31], the topological system offers advantages such as stability, efficiency, and parity control. Moreover, the topological refraction can be generated using a point source in the domain wall, while the generation of anomalous refraction with metamaterials relies on the input field. With high efficiency and stability, the topological refraction brings about promising applications for directional antennas [32].

In this paper, we experimentally demonstrate the topological transport and refraction via a sonic crystal with a Kekulé lattice. The Kekulé lattice introduces an alternative type of pseudospin that emerges from band folding. We observe the pseudospin-polarized topological effects, including the topologically protected edge states and the refraction of edge states into the ambient space. Either pseudospin-Hall or valley-Hall topological edge states are found in the Fourier spectrum depending on the type of internal domain wall. The outcoupled edge states from different terminations generate one beam, two beams in symmetric or antisymmetric fashion, or multibeams. The

*schen@nankai.edu.cn

odd or even parity of the outcoupled field is determined by the terminal interface, which has never been demonstrated before with acoustic topological edge modes. The azimuthal rule of the outcoupled field is explained by applying the phase-matching condition to the terminal interface. The experimental data agree fairly well with the two-dimensional full-wave simulations performed by COMSOL MULTIPHYSICS. With promising applications for directional antennas, the topological refraction may be exploited in acoustic detection, imaging, and underwater communication [26,33].

II. DESIGN

A. Tight-binding model

The Kekulé lattice is defined as a honeycomb lattice with Kekulé distortion. To study the sonic crystal in a Kekulé lattice, we employ a tight-binding model that includes interatomic interactions with nearest neighbors and next-nearest neighbors. The result of the tight-binding model is similar to the longitude branches of the spring model proposed in phonon systems [34,35]. The

Hamiltonian of the tight-binding model is [22]

$$H = \sum_i \varepsilon_i c_i c_i^\dagger + \sum_{\langle i,j \rangle, \langle\langle i,j \rangle\rangle} (t_{ij} c_i c_j^\dagger + \text{H.c.}), \quad (1)$$

where c and c^\dagger are the annihilation and creation operators on the lattice sites. The subscripts (i,j) represent the position of the lattice sites. The first term represents the on-site energy, where ε_i is equal on each sublattice site. The second term represents the interaction between nearest neighbors and next-nearest neighbors. In the real acoustic system as shown in Fig. 1(a), the atoms of the Kekulé lattice are virtual, as denoted with red dashed circles. The nearest-neighbor hopping $t_{a,b,c}$ and the next-nearest-neighbor hopping $t_{d,e,f}$ are denoted with arrows. The sonic crystal is a composite of two interlaced triangular lattices with the same lattice constants. The unit cell of rigid rods is embedded in an air background, with a radius of $r_A = 0.173a$ and $r_B = 0.260a$, where $a = 6$ cm is the lattice constant. The rods form the supercell of the Kekulé lattice. The atoms are connected with air and the vibration of one atom can interact with others through acoustic waves. The Kekulé distortion takes place if $t_{a,b,c}$ are not all

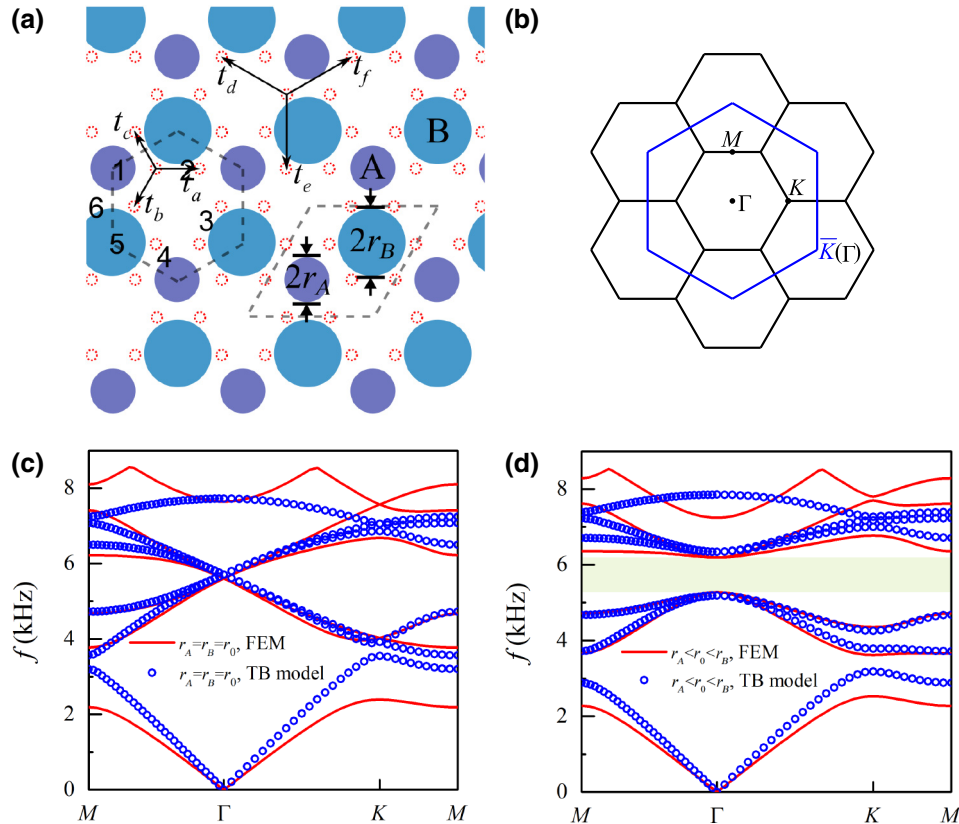


FIG. 1. (a) Schematic of the sonic crystal with the unit cell of two rigid rods embedded in an air background. For example, A and B rods in the dashed rhomboid or dashed hexagon. $t_{a,b,c,d,e,f}$ are the hopping between the virtual atoms denoted with red dashed circles. (b) The Brillouin zone (BZ) of the sonic crystal (black) and the original BZ of the hopping sites in the tight-binding model (blue). (c),(d) Bulk dispersions for the cases (c) $\delta r = 0$ and (d) $\delta r \neq 0$. The numerical result of the finite-element method (FEM) (red lines) is compared with the fitting results of the tight-binding (TB) model (blue circles).

equaled. By adding Kekulé distortion to the original honeycomb lattice, the corners of the original Brillouin zone (BZ) (\bar{K} and \bar{K}') are folded to the center of the new BZ (Γ) [Fig. 1(b)]. The real sonic crystal preserves the symmetry of the tight-binding model. The interaction strengths between a specific atom and three nearest atoms are generally different, because the symmetry operations of the sonic crystal would not transform one hopping path into another. The corresponding Bloch Hamiltonian $H(\mathbf{k})$ is given by

$$H(\mathbf{k}) = E_0 + \sum_{\langle ij \rangle, \langle\langle ij \rangle\rangle} (t_{i,j} e^{-i\mathbf{k}\cdot\mathbf{r}_{ij}} + \text{H.c.}), \quad (2)$$

where $E_0 = t_a + t_b + t_c - 2(t_d + t_e + t_f)$ is the on-site energy. Let us begin with a honeycomb lattice without Kekulé distortion ($t_a = t_b = t_c = t_1$). Double Dirac cones are formed at the Γ point of the BZ [Fig. 1(c)]. By fitting the simulation results, the parameters of the tight-binding model are $t_1 = 9.94$ and $t_d = -0.92$ in arbitrary units assuming $t_e = t_f = 0$. The interactions of next-nearest neighbors are considered, otherwise the double Dirac cones will degenerate into one Dirac cone. The interactions of next-nearest neighbor t_e and t_f are not considered, because the hopping path is blocked by the structure and the interactions are weak.

The eigenvectors of the Dirac cones are derived as

$$\begin{aligned} \Gamma_1 &= \frac{1}{\sqrt{6}}(e^{-2i\pi/3}, 0, 1, 0, e^{2i\pi/3}, 0)^T, \\ \Gamma_2 &= \frac{1}{\sqrt{6}}(0, e^{2i\pi/3}, 0, 1, 0, e^{-2i\pi/3})^T, \\ \Gamma_3 &= \Gamma_1^*, \\ \Gamma_4 &= \Gamma_2^*. \end{aligned} \quad (3)$$

Similar to the Dirac phonon eigenmodes in phonon system [34], the eigenvectors are also eigenstates of C_3 whose eigenvalues are $e^{2i\pi j_{\text{ph}}}$, where the phonon pseudoangular momenta $j_{\text{ph}} = +1$ for Γ_2, Γ_3 and $j_{\text{ph}} = -1$ for Γ_1, Γ_4 .

The Kekulé distortion introduces a perturbation term in the zeroth order of \mathbf{k} . In the basis of $(\Gamma_1, \Gamma_2, \Gamma_3, \Gamma_4)$, the perturbation effective Hamiltonian is

$$\begin{aligned} H_K &= (\Gamma_1, \Gamma_2, \Gamma_3, \Gamma_4)^\dagger H(\Gamma_1, \Gamma_2, \Gamma_3, \Gamma_4) - E_D \\ &= \Delta_0 + \Delta_1 \tau_x \sigma_x + \Delta_2 \tau_y \sigma_x = \Delta_0 + m_K \tau_n \sigma_x \end{aligned} \quad (4)$$

where $\Delta_0 = \Delta t_a + \Delta t_b + \Delta t_c$, $\Delta_1 = \Delta t_a - \Delta t_b/2 - \Delta t_c/2$, $\Delta_2 = \sqrt{3}(\Delta t_c - \Delta t_b)/2$, $E_D = 3t_1 - 3(t_d + t_e + t_f)$ is the Dirac energy, $m_K = \pm |m_K| = \pm(\Delta_1^2 + \Delta_2^2)^{1/2}$ and $m_K(\text{I}) = -m_K(\text{II})$ for the two domains, $\tau_n = \tau_x \sin \theta + \tau_y \cos \theta$ with the azimuthal angle $\theta \in (-\pi/2, \pi/2]$. With Kekulé distortion, the doubly degenerate Dirac point is lifted and a bandgap emerge [Fig. 1(d)]. The fitting parameters of the tight-binding model are $t_a = 9.1$, $t_b = 14.2$,

$t_c = 6.7$ and $t_d = -1.5$ in arbitrary units. The results of tight-binding model are in great accordance with the numerical simulation in the second and third bands, while in higher bands, the higher-order modes may occur, which are beyond the prediction of the tight-binding model. The phonon pseudospins of the Kekulé lattice are defined as [34]

$$\begin{aligned} E_{1,\uparrow} &= \frac{1}{\sqrt{2}}(ie^{i\theta}\Gamma_3 + i\Gamma_2), \\ E_{1,\downarrow} &= \frac{1}{\sqrt{2}}(\Gamma_1 + e^{i\theta}\Gamma_4), \\ E_{2,\uparrow} &= \frac{1}{\sqrt{2}}(\Gamma_1 - e^{i\theta}\Gamma_4), \\ E_{2,\downarrow} &= \frac{1}{\sqrt{2}}(-ie^{i\theta}\Gamma_3 + i\Gamma_2). \end{aligned} \quad (5)$$

When m_K is small, the pseudospin Chern number is quantized as $C_s = \pm(s/2)\text{sgn}(m_K)$, where $s = \pm 1$ is the eigenvalue of pseudospins, which represents pseudospin up or down. The domain wall with opposite m_K on the two sides leads to $\Delta C_s = \pm 1$, which may cause the quantum-spin-Hall-like states.

B. Sonic crystal with Kekulé distortion

To design a sonic crystal with Kekulé distortion, we start with a honeycomb lattice of rods that support the double Dirac cones. The doubly degeneracy requires a carefully chosen rod radius of $r_0 = r_A = r_B = 0.227a$. The double Dirac point is supported by the C_{6v} group symmetry, which has two two-dimensional irreducible representations. When $r_{A(B)} \neq r_0$, a complete band gap appears due to the reduced inversion symmetry caused by Kekulé distortion [Fig. 1(d)]. Specifically, we choose $r_A < r_0 < r_B$ as one topological domain (referred to as domain I) and swap the radius of A/B rods for the other domain (referred to as domain II). The band degeneracy at the double Dirac cones is lifted and the point group symmetry reduced to C_{3v} . The Dirac cones are hybridized by the p -orbital-like symmetric (S_1) mode and antisymmetric (A_1) mode, as well as the d -orbital-like symmetric (S_2) mode and antisymmetric (A_2) mode [Fig. 2(a)]. These symmetric and antisymmetric modes are similar with those in the phononic honeycomb lattice with C_{6v} symmetry [15]. For frequencies in the proximity of the original double Dirac cone, these hybridized eigenmodes can efficiently emulate new pseudospin and pseudospin states. Here we alter the radius of the two rods with distortion amplitude denoted by δr with $r_A = r_0 + \delta r$, $r_B = r_0 - \delta r$. Figure 2(b) plots the frequency spectra of states at Γ as a function of δr . With the increase of δr , the frequencies of A_1, S_1 boost while the frequencies of A_2, S_2 drop. The states exchange at the critical point of $\delta r = 0$. When we swap the big rods with small rods, the band dispersions of A_1, S_1 and A_2, S_2

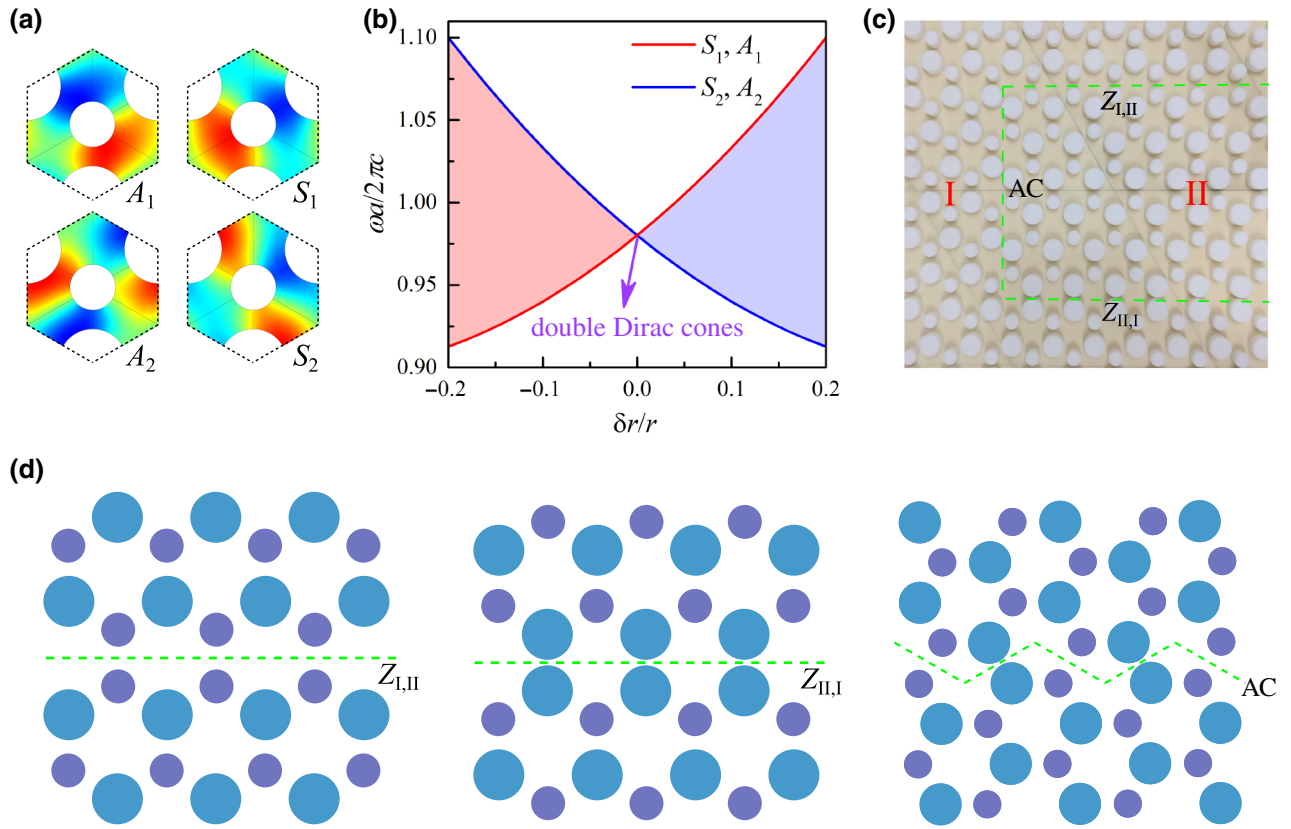


FIG. 2. (a) Simulated eigenfield profiles for A_1 , S_1 , A_2 , and S_2 states. (b) Frequency spectra of A_1 , S_1 , A_2 , and S_2 states at Γ as a function of the inversion-asymmetry amplitude δr with $r_A = r_0 + \delta r$, $r_B = r_0 - \delta r$. (c) Experimental setup with two domains I and II, forming zigzag interfaces $Z_{I,II}$, $Z_{II,I}$ and armchair (AC) interface (dashed green lines). (d) Schematic of the $Z_{I,II}$, $Z_{II,I}$, and AC interfaces.

exchange. By varying the radius of rods, the topological phase transition is either caused by inversion symmetry breaking or tuning the filling ratio, as shown in Fig. S1 within the Supplemental Material [36].

C. Pseudospin-polarized edge states

We can construct different kinds of domain wall between two domains that have opposite pseudospin Chern numbers. As shown in Figs. 2(c) and 2(d), the domain wall can be zigzag or armchair shaped. When the upper domain is domain I while the downer domain is domain II, zigzag domain wall with small rods near the boundary is formed (denoted as $Z_{I,II}$). As we swap the order of the two domains, another zigzag domain wall with big rods near the boundary is formed (denoted as $Z_{II,I}$). Because of the topological phase transition, a pair of edge states emerge within the overlapped bulk band gap of two different domains, as shown in Figs. 3(a) and 3(d). We note that these domain walls do not violate the hexagonal structures of atoms, otherwise the pseudospin-Hall edge states might not occur as discussed later. The phase distributions around the rods in each domain are measured as shown in Fig. S2 within the Supplemental Material, indicating that the two domains have different pseudospins [36].

From the pressure distributions scanned along the direction of domain walls, we obtain the corresponding dispersion spectra through a Fourier transform [Figs. 3(b), 3(c), 3(e), and 3(f)]. The experimental data (bright color) suit the numerical dispersions well (green dotted lines). Because of the reflection at the output terminal interface, the edge states contain its time-reversal counterparts. For $Z_{I,II}$, the amplitude distribution along the testing line is weak [Fig. 3(b)]. Therefore, we give the result with amplitude normalization over frequencies that the dispersions of edge states are obviously visualized [Fig. 3(c)].

Different kinds of not spin-mixing defects including cavity, disorder, and sharp bends are introduced into our topological waveguide to study the robustness of our acoustic topological edge states, as shown in Figs. 4(a)–4(c) with simulated acoustic pressure field. The sound source is placed at the left channel. The transmissions derived by the scattering matrix method [28] show that the topological waveguide can effectively detour around these defects with high transmission [Fig. 4(d)]. The gray-shaded area denotes the mini bandgap between 5634 and 5674 Hz, where the scattering matrix method is not available in this range. In the scattering matrix method, the defects can be considered as black boxes connecting the left (L) and right (R) channels. The acoustic incident waves p_L^+ , p_R^- (+ and

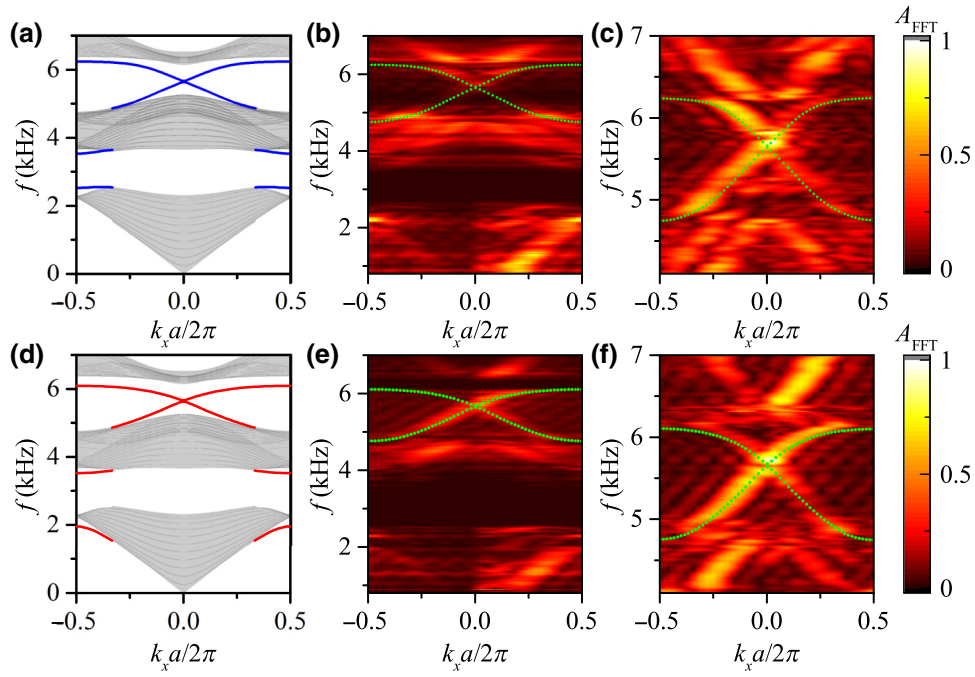


FIG. 3. Numerical and experimental validations of the topological edge modes. Band dispersions for the (a)–(c) $Z_{I,II}$ and (d)–(f) $Z_{II,I}$. (a),(d) Simulated by a superlattice structure containing two different horizontal domain walls. (b),(c),(e),(f) Experimentally measured dispersions (bright color) for the edge with numerical data (green dotted lines) (b),(e) without or with (c),(f) amplitude normalization over frequencies.

– denote the forward and backward traveling waves) and scattering waves p_L^- , p_R^+ are related by scattering matrix S through

$$\begin{pmatrix} p_L^- \\ p_R^+ \end{pmatrix} = S \begin{pmatrix} p_L^+ \\ p_R^- \end{pmatrix}. \quad (6)$$

In a dissipation-free system,

$$S = \begin{pmatrix} r & t \\ t & -r^*t/t^* \end{pmatrix}, \quad (7)$$

where r and t are the reflection and transmission coefficients. The scattering matrix can be solved in terms

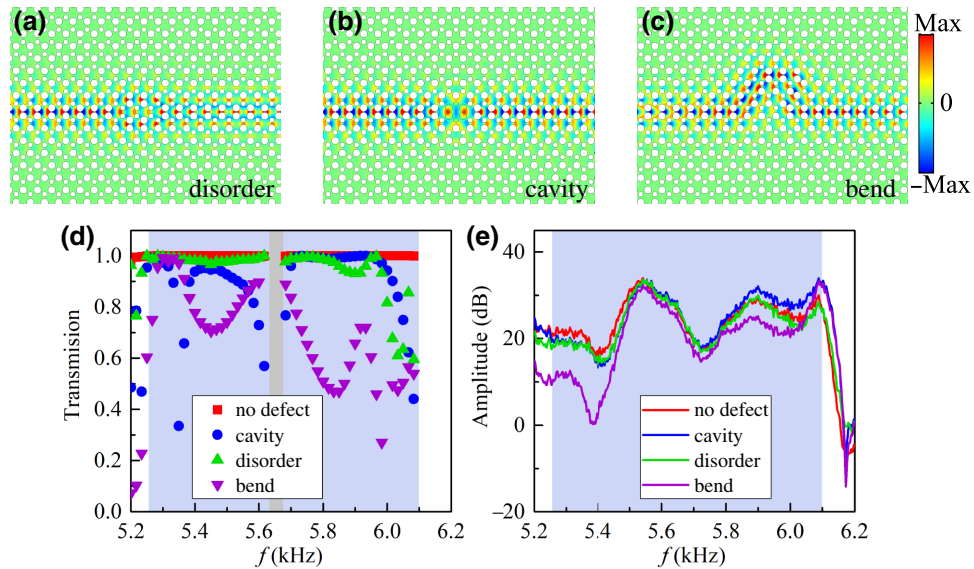


FIG. 4. Simulated acoustic pressure field distribution at 5.6 kHz with (a) disorder, (b) cavity, and (c) bend. (d) Simulated transmission and (e) measured amplitude for different configuration of defects, in contrast to configuration of no defects.

of p_L^\pm and p_R^\pm to calculate the transmission $T = |t|^2$. In Fig. 4(e), the experimental amplitudes measured at the right channel are $|p| = |p_R^- + p_R^+|$. When the reflection at the right terminal interface of the sonic crystal is negligible ($|p_R^+| \gg |p_R^-|$), we can obtain $|p| \approx |p_R^+| = |t \times p_L^+|$, and the experimental amplitudes can be directly related with the transmission. The transmission and the measured amplitude with defect of the sharp bends are both low around 5.4 and 5.9 kHz in contrast to other kinds of defects, as the reflection at the terminal interface is about 0.1~0.2 (see Fig. S3 within the Supplemental Material [36]), which can be neglected in coarse analysis. The intrinsic loss of airborne sound also influences the amplitude, which is measured by fitting the exponential function as shown in Fig. S4 within the Supplemental Material [36]. The transmissions of edge states at crossing zigzag or armchair interfaces are shown in Fig. S5 within the Supplemental Material [36].

D. Topological directional antenna

When the Bloch wave is coupled to the outer space, the refraction angles are interpreted by the phase-matching conditions at the terminations, as shown in Figs. 5(a) and 5(b). The waveguide dispersions (illustrated by

circles) are the same as the free space: $k_0 = \omega/c$, where the sound velocity of air is $c = 343$ m/s. The output wave vectors \mathbf{k}_{out} are locked to equivalent Γ point of the nearest-neighbor BZ. For armchair terminations, the output wave vectors \mathbf{k}_{out} satisfy $\mathbf{k}(\Gamma \rightarrow \Gamma_{\text{NN}}) \cdot \mathbf{e}_x = \mathbf{k}_{\text{out}} \cdot \mathbf{e}_x$. As graphically solved in Fig. 5(a), two solutions can be found with reflection symmetry about the k_y axis. For zigzag termination, only the zero-order refraction branch is found due to the phase matching along \mathbf{e}_x . However, the zigzag termination allows another phase-matching condition along $\pm \cos(\pi/6)\mathbf{e}_x + \sin(\pi/6)\mathbf{e}_y$, which arouses two side branches, as illustrated in Fig. 5(b). Because of the reflection symmetry of the two domains, the edge states of zigzag edge must be symmetric or antisymmetric. Experimentally scanned outer-space field patterns are plotted in Figs. 5(c)–5(e) with comparison of simulation results in Figs. 5(f)–5(h). With zigzag domain walls and armchair terminations, the edge modes of odd or even parity refract into two directional beams, whereas three directional beams appear with zigzag termination. The theoretical predictions agree with the simulation and experiment results. In previous works, the symmetric and antisymmetric beam generation can only be found in metasurfaces that relies on the input field and accompany with transmission loss. Utilizing the topological refraction, the

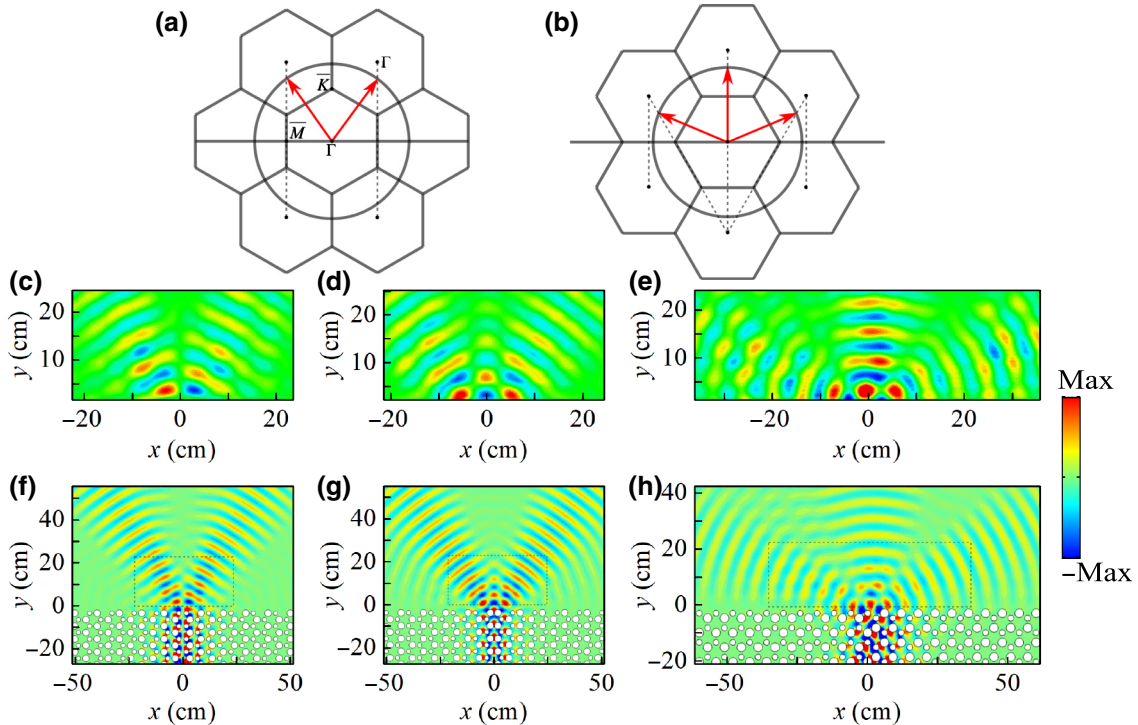


FIG. 5. Topologically protected refraction of pseudospin-Hall states into an empty waveguide region. (a),(b) The \mathbf{k} -space analysis on the outcoupling of (a) armchair termination at $f = 5.6$ kHz, and (b) zigzag terminations at $f = 5.8$ kHz. Circles represent the dispersions of a free-space \mathbf{k} vector. Red arrows represent all possible outcoupling directions. (c)–(e) Measurements and (f)–(h) simulations of the refraction through (c),(d),(f),(g) zigzag domain walls and armchair terminations, (e),(h) the armchair domain wall and the zigzag termination. The edge states and outcoupling fields possess (c),(f) odd and (d),(g) even parity for the $Z_{I,II}$ and $Z_{II,I}$ domain wall, respectively.

symmetric and antisymmetric beam can be generated with any kind of input source. Meanwhile, the transmission loss can be reduced and the results are more stable. The angle resolved far-field patterns of outcoupling waves are shown in Supplemental Material Fig. S6 [36], exhibiting high-directivity performances.

E. Valley states and interface-dependent edge states

The valley states also emerge in the Kekulé lattice if the nearest-neighbor hopping is $t_a \neq t_b \neq t_c$ in the tight-binding model. The tight-binding model only gives a rough estimation to the lowest band dispersion in Figs. 1(c) and 1(d). The effect of the cavities with each surrounded by six rods are not considered in the tight-binding model. The cavity resonance is strong at the lowest band [see strong amplitudes in Fig. 5(c)], which makes the dispersion lower than the estimation from the tight-binding model. If we remove the small rods, a triangular lattice is formed so that a twofold Dirac degeneracy is protected at $K(K')$ with C_{3v} symmetry [Fig. 6(a), black lines]. In this case, the Dirac degeneracy is lifted by inserting the small rods into the lattice of only the big rods (see Fig. S7 within the

Supplemental Material [36]), which causes the C_{3v} point group symmetry to reduce to C_3 at K [Fig. 6(a), red and blue lines]. The valley vortexes are centered at the two inequivalent triangular-lattice centers p and q [Fig. 6(b)]. Here we show the eigenfield profiles for the K states ψ_{p^-} and ψ_{q^+} in Figs. 6(c) and 6(d), which are in accordance with previous works [21,37]. The sign \pm indicates an anticlockwise or clockwise energy flow.

The valley transport arises between the first and second band with zigzag domain walls $Z'_{I,II}$ and $Z_{II,I}$ as schematically shown in Fig. 7(a). The bulk bands are projected to ΓK direction with the $K(K')$ valleys projected on the edge with $k_x = \pm 4\pi/(3a)$. The edge states emerge between the upper and downer valleys. The group velocities of the edge states are in opposite directions for different valleys [Fig. 7(b)]. In this case, the big (small) rods form a triangular lattice in the domains and the small (big) rods are treated as distortion of the triangular lattice. Here we show the experimental measurement [Figs. 7(c) and 7(d)] compared with the simulation [Figs. 7(e) and 7(f)]. The output waves are vertical to the armchair termination since the wave vectors are locked to K , although the parities of $Z'_{I,II}$ and $Z_{II,I}$ edge modes are odd and even, respectively. The

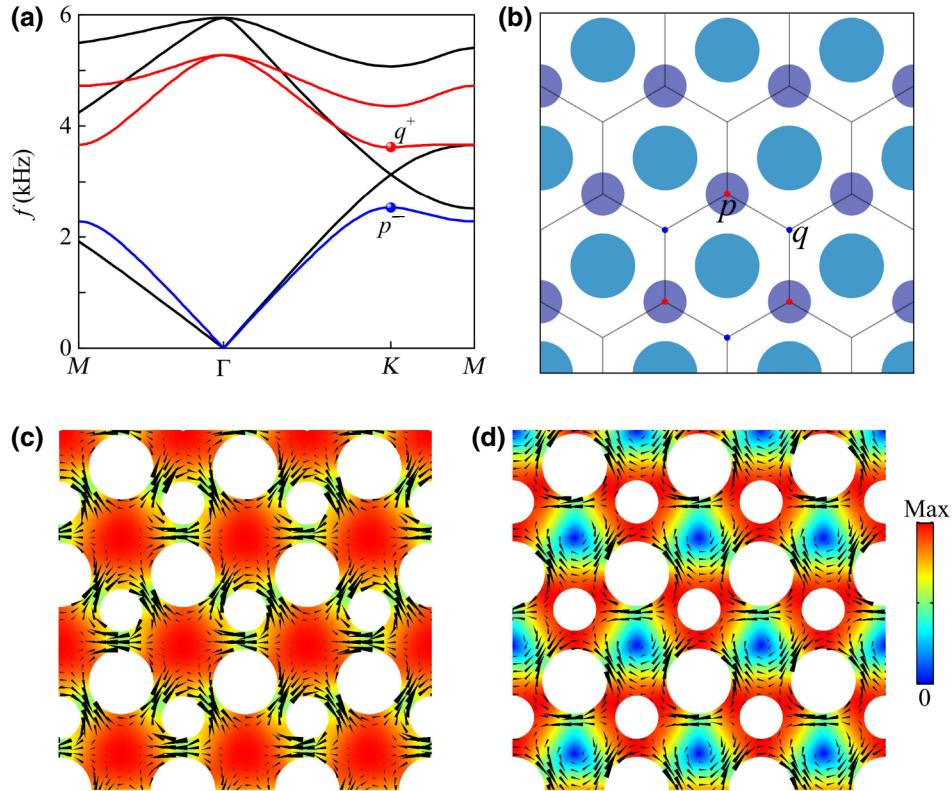


FIG. 6. (a) Gapless and gapped bulk dispersions for the sonic crystals with (color lines) or without the small rods (black lines). (b) Schematic of the sonic crystal where p and q indicate two inequivalent triangular-lattice centers. (c)–(d) Simulated eigenfield for the degenerate K states (c) ψ_{p^-} and (d) ψ_{q^+} . The pressure amplitudes are shown by colors. The energy flows (black cones) show distinct vorticities surrounding the points p and q .

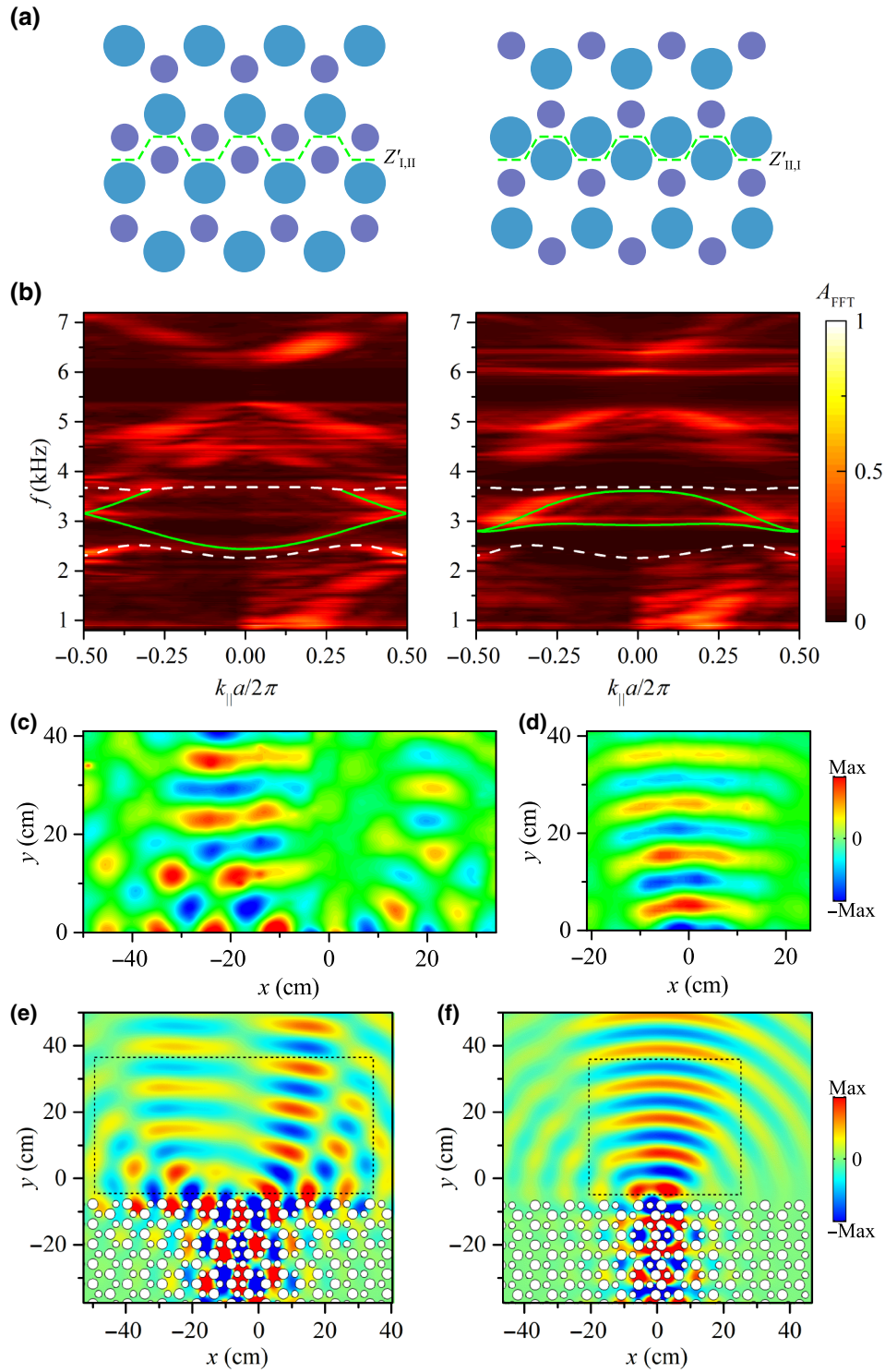


FIG. 7. Schematic for domain walls (a) $Z'_{I,II}$ and (b) $Z'_{II,I}$. (b) Band dispersions of domain walls $Z'_{I,II}$ (left) and $Z'_{II,I}$ (right). Experimental measured dispersions using Fourier transform are in bright color and the simulated result are the green lines. (c),(d) Measurements and (e),(f) simulations of the refraction through (c),(e) $Z'_{I,II}$, (d),(f) $Z'_{II,I}$ with armchair terminations. The \mathbf{k} vector is around the projection of K point with $f = 2.8$ kHz for $Z'_{I,II}$ and $f = 3.3$ kHz for $Z'_{II,I}$.

output angles slightly deviate from the theoretical analysis, because the fine structures of terminations may also affect the output angles. The pseudospin-Hall edge states vanish

as the domain wall violates the hexagonal structure of atoms, while the big or small rods form a triangular lattice, which ensures the valley-Hall transport.

III. CONCLUSION

In conclusion, we theoretically and experimentally investigate acoustic topological transport and refraction in a Kekulé lattice. We determine the existence of edge states by measuring the dispersion at domain walls. Exotic topological refraction of output wave in free space is observed. The edge states of the sonic crystal are interface dependent, exhibiting either pseudospin-Hall or valley-Hall transport, which greatly varies the domain-wall design. The topological system offers advantages such as stability, efficiency, and parity control for the application of acoustic beam splitters. This concept is also expected to inspire antenna designs in both acoustics and photonics.

ACKNOWLEDGMENTS

This work is supported by the National Key Research and Development Program of China (Grants No. 2016YFA0301102 and No. 2017YFA0303800); National Natural Science Foundation of China (Grants No. 91856101, No. 11774186, and No. 11574163); Natural Science Foundation of Tianjin for Distinguished Young Scientists (Grant No. 18JCQJC45700); Natural Science Foundation of Tianjin (Grant No. 16JCQNJC01700), and 111 Project (B07013).

-
- [1] Yiqun Ding, Zhengyou Liu, Chunyin Qiu, and Jing Shi, Metamaterial with Simultaneously Negative Bulk Modulus and Mass Density, *Phys. Rev. Lett.* **99**, 093904 (2007).
- [2] Zixian Liang and Jensen Li, Extreme Acoustic Metamaterial by Coiling Up Space, *Phys. Rev. Lett.* **108**, 114301 (2012).
- [3] Fengming Liu, Xueqin Huang, and C. T. Chan, Dirac cones at $\vec{k} = 0$ in acoustic crystals and zero refractive index acoustic materials, *Appl. Phys. Lett.* **100**, 071911 (2012).
- [4] B. Liang, X. S. Guo, J. Tu, D. Zhang, and J. C. Cheng, An acoustic rectifier, *Nat. Mater.* **9**, 989 (2010).
- [5] Xue-Feng Li, Xu Ni, Liang Feng, Ming-Hui Lu, Cheng He, and Yan-Feng Chen, Tunable Unidirectional Sound Propagation through a Sonic-Crystal-Based Acoustic Diode, *Phys. Rev. Lett.* **106**, 084301 (2011).
- [6] Tuo Liu, Xuefeng Zhu, Fei Chen, Shanjun Liang, and Jie Zhu, Unidirectional Wave Vector Manipulation in Two-Dimensional Space with an All Passive Acoustic Parity-Time-Symmetric Metamaterials Crystal, *Phys. Rev. Lett.* **120**, 124502 (2018).
- [7] J. Zhu, J. Christensen, J. Jung, L. Martin-Moreno, X. Yin, L. Fok, X. Zhang, and F. J. Garcia-Vidal, A holey-structured metamaterial for acoustic deep-subwavelength imaging, *Nat. Phys.* **7**, 52 (2010).
- [8] Lucian Zigoneanu, Bogdan-Ioan Popa, and Steven A. Cummer, Three-dimensional broadband omnidirectional acoustic ground cloak, *Nat. Mater.* **13**, 352 (2014).
- [9] Nanfang Yu, Patrice Genevet, Mikhail A. Kats, Francesco Aieta, Jean-Philippe Tetienne, Federico Capasso, and Zeno Gaburro, Light propagation with phase discontinuities: Generalized laws of reflection and refraction, *Science* **334**, 333 (2011).
- [10] Yangbo Xie, Wenqi Wang, Huanyang Chen, Adam Konneker, Bogdan-Ioan Popa, and Steven A. Cummer, Wavefront modulation and subwavelength diffractive acoustics with an acoustic metasurface, *Nat. Commun.* **5**, 5553 (2014).
- [11] Daniel Torrent and José Sánchez-Dehesa, Acoustic Analogue of Graphene: Observation of Dirac Cones in Acoustic Surface Waves, *Phys. Rev. Lett.* **108**, 174301 (2012).
- [12] Xiangdong Zhang and Zhengyou Liu, Extremal Transmission and Beating Effect of Acoustic Waves in Two-Dimensional Sonic Crystals, *Phys. Rev. Lett.* **101**, 264303 (2008).
- [13] Zhaoju Yang, Fei Gao, Xihang Shi, Xiao Lin, Zhen Gao, Yidong Chong, and Baile Zhang, Topological Acoustics, *Phys. Rev. Lett.* **114**, 114301 (2015).
- [14] Alexander B. Khanikaev, Romain Fleury, S. Hossein Mousavi, and Andrea Alù, Topologically robust sound propagation in an angular-momentum-biased graphene-like resonator lattice, *Nat. Commun.* **6**, 8260 (2015).
- [15] Cheng He, Xu Ni, Hao Ge, Xiao-Chen Sun, Yan-Bin Chen, Ming-Hui Lu, Xiao-Ping Liu, and Yan-Feng Chen, Acoustic topological insulator and robust one-way sound transport, *Nat. Phys.* **12**, 1124 (2016).
- [16] Zhiwang Zhang, Qi Wei, Ying Cheng, Ting Zhang, Dajian Wu, and Xiaojun Liu, Topological Creation of Acoustic Pseudospin Multipoles in a Flow-Free Symmetry-Broken Metamaterial Lattice, *Phys. Rev. Lett.* **118**, 084303 (2017).
- [17] G. Q. Liang and Y. D. Chong, Optical Resonator Analog of a Two-Dimensional Topological Insulator, *Phys. Rev. Lett.* **110**, 203904 (2013).
- [18] Yu-Gui Peng, Cheng-Zhi Qin, De-Gang Zhao, Ya-Xi Shen, Xiang-Yuan Xu, Ming Bao, Han Jia, and Xue-Feng Zhu, Experimental demonstration of anomalous Floquet topological insulator for sound, *Nat. Commun.* **7**, 13368 (2016).
- [19] Qi Wei, Ye Tian, Shu-Yu Zuo, Ying Cheng, and Xiaojun Liu, Experimental demonstration of topologically protected efficient sound propagation in an acoustic waveguide network, *Phys. Rev. B* **95**, 094305 (2017).
- [20] Jiuyang Lu, Chunyin Qiu, Manzhu Ke, and Zhengyou Liu, Valley Vortex States in Sonic Crystals, *Phys. Rev. Lett.* **116**, 093901 (2016).
- [21] Bai-Zhan Xia, Ting-Ting Liu, Guo-Liang Huang, Hong-Qing Dai, Jun-Rui Jiao, Xian-Guo Zang, De-Jie Yu, Sheng-Jie Zheng, and Jian Liu, Topological phononic insulator with robust pseudospin-dependent transport, *Phys. Rev. B* **96**, 094106 (2017).
- [22] Meng Xiao, Wen-Jie Chen, Wen-Yu He, and C. T. Chan, Synthetic gauge flux and Weyl points in acoustic systems, *Nat. Phys.* **11**, 920 (2015).
- [23] Feng Li, Xueqin Huang, Jiuyang Lu, Jiahong Ma, and Zhengyou Liu, Weyl points and Fermi arcs in a chiral phononic crystal, *Nat. Phys.* **14**, 30 (2017).
- [24] Boyang Xie, Hui Liu, Hua Cheng, Zhengyou Liu, Shuqi Chen, and Jianguo Tian, Experimental Realization of Type-II Weyl Points and Fermi Arcs in Phononic Crystal, *Phys. Rev. Lett.* **122**, 104302 (2019).

- [25] Valerio Peri, Marc Serra-Garcia, Roni Ilan, and Sebastian D. Huber, Axial-field-induced chiral channels in an acoustic Weyl system, *Nat. Phys.* **15**, 357 (2019).
- [26] Fei Gao, Haoran Xue, Zhaoju Yang, Kueifu Lai, Yang Yu, Xiao Lin, Yidong Chong, Gennady Shvets, and Baile Zhang, Topologically protected refraction of robust kink states in valley photonic crystals, *Nat. Phys.* **14**, 140 (2017).
- [27] Jian-Wen Dong, Xiao-Dong Chen, Hanyu Zhu, Yuan Wang, and Xiang Zhang, Valley photonic crystals for control of spin and topology, *Nat. Mater.* **16**, 298 (2016).
- [28] Jiuyang Lu, Chunyin Qiu, Liping Ye, Xiying Fan, Manzhu Ke, Fan Zhang, and Zhengyou Liu, Observation of topological valley transport of sound in sonic crystals, *Nat. Phys.* **13**, 369 (2016).
- [29] Liping Ye, Chunyin Qiu, Jiuyang Lu, Xinhua Wen, Yuanyuan Shen, Manzhu Ke, Fan Zhang, and Zhengyou Liu, Observation of acoustic valley vortex states and valley-chirality locked beam splitting, *Phys. Rev. B* **95**, 174106 (2017).
- [30] Ma Tzuhsuan and Shvets Gennady, All-Si valley-Hall photonic topological insulator, *New J. Phys.* **18**, 025012 (2016).
- [31] J. Bucay, E. Roussel, J. O. Vasseur, P. A. Deymier, A.-C. Hladky-Hennion, Y. Pennec, K. Muralidharan, B. Djafari-Rouhani, and B. Dubus, Positive, negative, zero refraction, and beam splitting in a solid/air phononic crystal: Theoretical and experimental study, *Phys. Rev. B* **79**, 214305 (2009).
- [32] Zhiwang Zhang, Ye Tian, Yihe Wang, Shuxiang Gao, Ying Cheng, Xiaojun Liu, and Johan Christensen, Directional acoustic antennas based on valley-hall topological insulators, *Adv. Mater.* **30**, 1803229 (2018).
- [33] Romain Fleury, Alexander B. Khanikaev, and Andrea Alù, Floquet topological insulators for sound, *Nat. Commun.* **7**, 11744 (2016).
- [34] Yizhou Liu, Chao-Sheng Lian, Yang Li, Yong Xu, and Wenhui Duan, Pseudospins and Topological Effects of Phonons in a Kekulé Lattice, *Phys. Rev. Lett.* **119**, 255901 (2017).
- [35] Yi Chen, Xiaoning Liu, and Gengkai Hu, Topological phase transition in mechanical honeycomb lattice, *J. Mech. Phys. Solids* **122**, 54 (2019).
- [36] See Supplemental Material at <http://link.aps.org/supplemental/10.1103/PhysRevApplied.11.044086> for (i) topological phase with varying radius, (ii) vortex around the domain wall, (iii) reflection at termination, (iv) measured decay along or vertical to the domain wall, (v) edge states at crossing channels, (vi) simulated outcoupling angle at different frequencies, (vii) evolution of valley edge states.
- [37] Jiuyang Lu, Chunyin Qiu, Manzhu Ke, and Zhengyou Liu, Valley Vortex States in Sonic Crystals, *Phys. Rev. Lett.* **116**, 093901 (2016).